Application of Mass Lumped Higher Order Finite Elements ⋆

J. Chen [a] H. R. Strauss [b] S. C. Jardin [a] W. Park [a]
L. E. Sugiyama [c] G. Fu [a] J. Breslau [a]

[a] *PPPL, P.O. Box 451, Princeton, NJ 08543*
[b] *Courant Institute, NYU, 251 Mercer Street, NY 10012*
[c] *Massachusetts Institute of Technology, Cambridge, MA 02139*

Abstract

There are many interesting phenomena in extended-MHD such as anisotropic transport, mhd, 2-fluid effects, stellarator and hot particles. Any one of them challenges numerical analysts, and researchers are seeking for higher order methods, such as higher order finite difference, higher order finite elements and hp/spectral elements. It is true that these methods give more accurate solution than their linear counterparts. However, numerically they are prohibitively expensive. Here we give a successful solution of this conflict by applying mass lumped higher order finite elements. This type of elements not only keep second/third order accuracy but also scale closely to linear elements by doing mass lumping. This is especially true for second order lump elements. Full M3D and anisotropic transport models are studied.

Key words: Higher order finite elements, mass lumping, highly anisotropic transport
1991 MSC: 74E10, 65N30

1. Introduction

The extended-MHD [1] [2] is rich in multilevel physics, such as anisotropic transport, mhd, 2-fluid effects, stellarator and hot particles. Among them, solving the highly anisotropic transport is difficult but fundamental. For such phenomena, the higher order methods, such as higher order finite difference [3], higher order finite elements [4] and hp/spectral elements [5] have become

⋆ This work is supported by US DoE contract DE-AC02-76CH03073.

more and more popular. Compared to linear methods [6] [7], these methods give more accurate solution, particularly when the grid is not parallel to the transport axis. Among them, the finite elements are well adapted to represent complex geometry. However, in the use of finite elements, continuously inverting the mass matrix presents a major drawback, and this is a fundamental factor to affect the numerical efficiency. For linear elements, mass lumping gives a good solution to the numerical performance. Nevertheless, this is much less obvious in the case of higher order finite elements.

In order to have the accuracy of higher order elements as well as keep the reasonable numerical efficiency of linear ones, the mass lumped higher order elements are introduced in [8] and implemented here by the authors in toroidal geometry. Compared to the Lagrange higher order elements, extra one bubble node is added in the second order ones and extra 2 bubble nodes are added in the third order ones, respectively (Figure 1). As a result, the number of collation points increases to be the same as the number of nodal points. These 2 sets of points are carefully arranged so that they coincide with each other. An extra third order term or fourth order term were added to each second or third order bases functions, and in the same time the integral weight was carefully chosen so that the Lagrange property

$$N_i(\alpha_j, \beta_j) = \delta_{ij} \tag{1}$$

are kept for the basis functions at the nodal point set as well as on the collation point set also. Here (α_j, β_j) are the values of barycentric coordinate (α, β) at the nodal points n_j. Therefore, mathematically these basis behave similarly to spectral elements with Gauss-Lobatto quadrature points, so that the mass matrix M remains to be diagonal. Now the mass lumping can be easily and accurately taken.

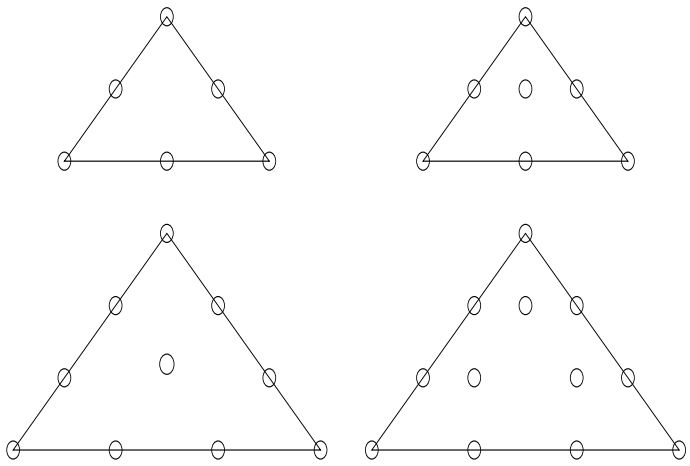

Fig. 1.

For simplicity, the Lagrange higher order elements are called Lagrange ho ele-

ments, while the higher order elements with mass lumping are called lump ho elements in this work. The Lagrange ho elements have already been installed in M3D [4] and here the lump ho elements is compatibly integrated into it. The numerical accuracy and efficiency of operators, such as first order derivative, gradient, Laplacian, inner product, and cross product, as well as elliptic solvers, such as Poisson equations and Helmholtz equations, are monitored in the process of solving realistic plasma modeling in section 2.

2. Numerical Accuracy and Efficiency Comparisons in M3D

M3D is a Multilevel, 3D code performing linear and non-linear calculations of plasmas in toroidal topologies including tokamaks and stellarators, ideal and resistive MHD models, two-fluid model, as well as hybrid particle-fluid. The poloidal plane is represented by unstructured triangular mesh, and 4th order finite difference is taken along toroidal direction.

Table 1: numerical accuracy

solvers/operators	linear	Lagrange ho	lump ho
$\Delta^{\perp}u = f^{\perp}$: u	.3133E-04	.1824E-10	.2778E-10
$\Delta^{\star}u = f^{\star}$: u	.7480E-04	.1741E-07	.9668E-11
$\Delta^{\dagger}u = f^{\dagger}$: u	.7689E-05	.1368E-07	.1316E-11
$(\Delta^{\perp} + \lambda I)u = f_h^{\perp}$: u	.8375E-04	.5808E-06	.5921E-11
$(\Delta^{\star} + \lambda I)u = f_h^{\star}$: u	.2019E-03	.1122E-04	.1187E-10
$(\Delta^{\dagger} + \lambda I)u = f_h^{\dagger}$: u	.3648E-04	.1582E-06	.1542E-10
$\Delta^{\perp}u = f^{\perp}$ (Neumann) : $\frac{\partial u}{\partial x}$	.3034E-02	.1049E-03	.1157E-03
: $\frac{\partial u}{\partial y}$	.2290E-02	.7860E-04	.8898E-04
$\frac{\partial u}{\partial x}$	.2424E-03	.7718E-11	.4413E-13
$\frac{\partial u}{\partial y}$	.9665E-03	.1709E-09	.2709E-13
$\frac{\partial^2 u}{\partial x \partial y} - \frac{\partial^2 u}{\partial y \partial x}$	.9787E-03	.1705E-09	.5611E-11
$v_1 \cdot v_2$	.4251E-03	.7760E-13	.4639E-13
$v_1 \times v_2$	.3830E-02	.6218E-09	.9326E-14
Laplacian	.6927E-03	.9690E-10	.1106E-09

In a full M3D run, we need to continuously invert stiffness matrices in the elliptic solvers and mass matrix in the derivative operators. There are seven type of elliptic solvers as listed in [9] and six types of derivative operators

listed below in Table 1. There are also other operators not listed here since they are more related to toroidal derivative, not directly related to higher order elements. At each time step there are $13 \sim 19$ elliptic solvers calls as well as hundreds of derivative operator calls involved.

Table 2: cpu time

solvers/operators	linear	Lagrange ho	lump ho
$\Delta^{\perp} u = f^{\perp}$	11.505164	17.993580	15.881487
$\Delta^{\star} u = f^{\star}$	11.936641	17.842965	15.577935
$\Delta^{\dagger} u = f^{\dagger}$	11.487363	17.065694	15.590550
$(\Delta^{\perp} + \lambda I)u = f_h^{\perp}$	11.593001	17.850698	15.764700
$(\Delta^{\star} + \lambda I)u = f_h^{\star}$	11.827986	17.617935	15.462633
$(\Delta^{\dagger} + \lambda I)u = f_h^{\dagger}$	11.127486	17.504207	15.329060
$\Delta^{\perp} u = f^{\perp}$ (Neumann)	11.800331	17.994744	15.368874
$\frac{\partial u}{\partial x}$	0.325041	2.822974	0.443981
$\frac{\partial u}{\partial y}$	0.467021	2.539099	0.469528
$\frac{\partial^2 u}{\partial x \partial y} - \frac{\partial^2 u}{\partial y \partial x}$	0.560459	9.457784	2.098601
$v_1 \cdot v_2$	0.680051	2.715444	0.961536
$v_1 \times v_2$	0.234130	2.418649	0.544330
Laplacian	0.355726	6.733015	0.554883

Here in the toroidal geometry, we are using approximately 7000 vertexes per poloidal plane to monitor the numerical accuracy and cpu time incurred by each solver/operator for the linear elements, Lagrange ho elements, and lump ho elements as well. Only 2nd order elements are considered in this comparison. The numerical accuracy given in Table 1 is measured against the exact solution. The first part of the table corresponds to the elliptic solvers : pure Poisson, star Poisson, dagger Poisson, Helmholtz pure Poisson, Helmholtz star Poisson, Helmholtz dagger Poisson, respectively. They are subject to Dirichlet b.c., and their definition can be found in [9]. The second part of the table gives the pure Poisson solver subjected to Neumann b.c. and the accuracies are given in the first order partial derivative $\frac{\partial}{\partial x}$ and $\frac{\partial}{\partial y}$ of the numerical solution due to a constant related to the uniqueness. The last part of the table gives the operators ranging from first order partial derivative $\frac{\partial}{\partial x}$ and $\frac{\partial}{\partial y}$, second order derivative commute $\frac{\partial^2}{\partial x \partial y} - \frac{\partial^2}{\partial y \partial x}$ related to the computation of $\nabla \cdot \mathbf{B}$ where $\mathbf{B}$ is the magnetic field, to vector inner product, cross product, and Laplacian as well. Obviously, the Lagrange ho elements beat the linear elements and lump ho elements inherit this property. In fact in most cases, the lump ho elements

have more accurate digits due to extra third and fourth order terms added in the their bases.

The corresponding cpu times to find the solutions from the solvers or form the operators, measured in seconds, are given in Table 2 in the same order. From the table it can immediately tell that the cpu time for the solvers has increased $\frac{1}{3}$ when switching from linear elements to Lagrange 2nd order elements, whereas this number is less than $\frac{1}{4}$ for lump 2nd order elements. The most significant and key improvement comes from operators given in the last part of the table. The Lagrange 2nd order elements take longer to run, some cases even 20 times more than the linear ones, while lump 2nd order elements scale to linear elements in most cases. This can be explained by the replacing of the mass matrix inversion in Lagrange ho elements completely by the vector point-wise division in lump ho elements due to mass lumping.

3. Model Tests

The full M3D run is a very complex system, involving advancing 7 equations explicitly or coupled implicitly or uncoupled implicitly at each time step. For simplicity, two highly anisotropic transport examples are taken as snapshots of M3D to demonstrate the characteristics of higher order elements. Here only lump ho elements are applied. Same conclusion can be made for Lagrange ho elements.

In both cases, the domains are 2D rectangle: ABCD: $[0, L_x] \times [0, L_y]$ (Figure 2). [AB] is aligned with the x-coordinate and [AD] is aligned with the y-coordinate. One has the strong transport direction aligned with the rectangle's diagonal; the other one has the magnetic field circular around the rectangle's center. They are realistic enough to modeling toroidal plasma. The linear, second, and third order elements are applied and their numerical behaviors are fully studied.

31 Case I

The model problem considered is the steady-state anisotropic heat conduction equation [3] in 2D:

$$\nabla \cdot (\vec{\kappa} \nabla T) = 0, \tag{2}$$

where T is the temperature and $\vec{\kappa}$ is the conductivity tensor. This can be written in the orthogonal coordinates (ξ, η), which are aligned with the transport

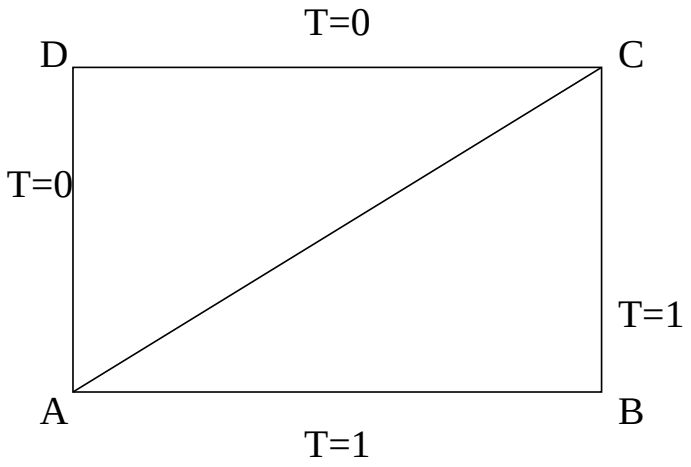

Fig. 2.

axes, as follows:

$$\frac{\partial}{\partial \xi}\kappa_\xi \frac{\partial T}{\partial \xi} + \frac{\partial}{\partial \eta}\kappa_\eta \frac{\partial T}{\partial \eta} = 0. \tag{3}$$

Without loss of generality we assume $\kappa_\xi \gg \kappa_\eta$, so that the strong transport direction is aligned with ξ.

The solution domain is given in the Cartesian coordinates (x, y), which are not aligned with the transport axes (ξ, η). There is an angle θ_m between the axis ξ and x. The Dirichlet boundary condition is shown in Fig. 1: T=0 on side [AD-DC] and T=1 on side [AB-BC], so that the strong transport axis ξ is parallel to the diagonal [AC]. For infinite anisotropy, the exact solution is: $T = 0$ above the grid diagonal [AC], $T = 1$ below the grid diagonal [AC], and the width of the transition zone is zero. For a finite anisotropy, the exact solution introduces an internal layer which has non-zero transition width (referred as profile width). We will show that the resolution of this layer depends on higher order elements when $\kappa_{||}$ is large.

32 Case II

The second example is a demonstration of the accurate calculation of anisotropic thermal conduction governed by equation:

$$\nabla \cdot \kappa_{||} \mathbf{BB} \cdot \nabla \Phi + \nabla \cdot \kappa \nabla \Phi + S(x, y) = 0 \tag{4}$$

in the existence of magnetic field $\mathbf{B}$ [10]. $\mathbf{B}$ is the 2D field written in terms of a given flux function $\psi(x, y)$, i.e., $\mathbf{B} = \hat{z} \times \nabla \psi$, and $\psi(x, y) = \sin \frac{\pi x}{L_x} \sin \frac{\pi y}{L_y}$. Therefore, $\mathbf{B}$ has a structure given in figure 3.

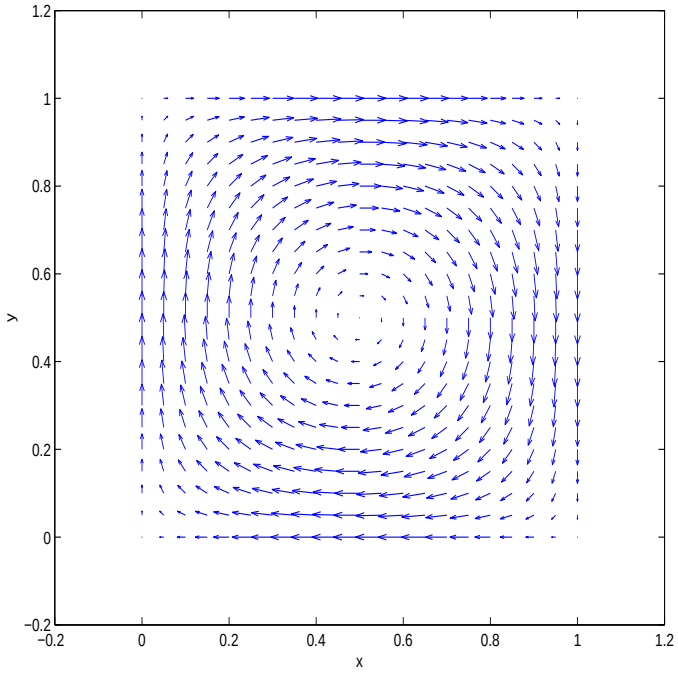

Fig. 3.

In this application we let $\kappa = 1, S(x, y) = \psi(x, y)$, and

$$\Phi = \frac{\sin \frac{\pi x}{L_x} \sin \frac{\pi y}{L_y}}{(\pi/L_x)^2 + (\pi/L_y)^2},$$

so that the solution should be independent of the value of the parallel conductivity $\kappa_{||}$. But It will be found that this can only be approximately achieved by higher order elements when $\kappa_{||}$ is large.

4. Mesh Setup

The unstructured triangular mesh is formed by first dividing the rectangular domain ABCD into uniform rectangular cells: $[0, N_x - 1] \times [0, N_y - 1]$. Then each of the rectangle grids is subdivided into two triangles in the following 3 ways:

- Mesh t1 in Figure 4.
  The strong transport direction ξ has full alignment with the element edge which is parallel to the diagonal [AC].
- Mesh t2 in Figure 4.
  The strong transport direction ξ has no alignment with the element edge. The elements, aligned with ξ in Mesh t1, are now aligned with the other diagonal [BD].

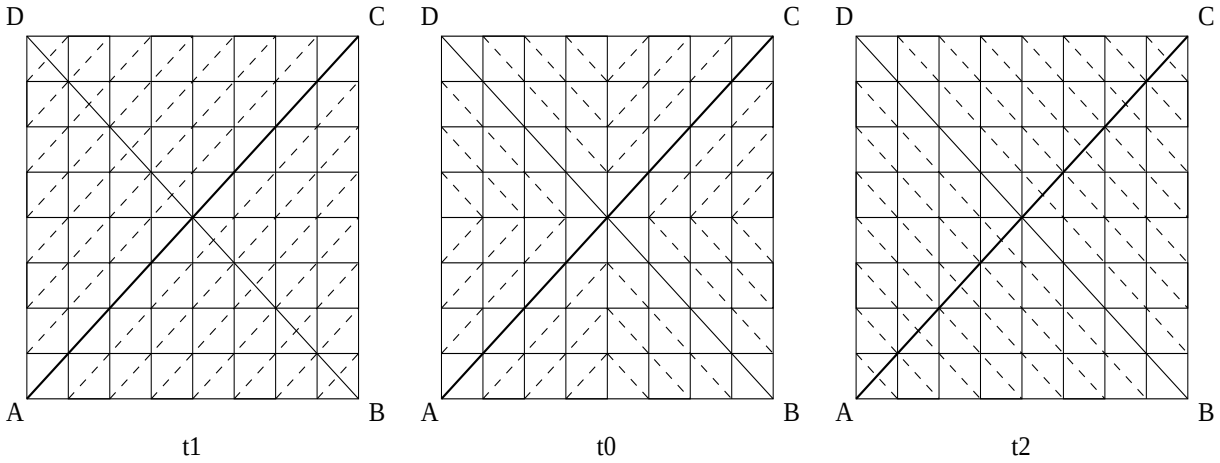

Fig. 4.

- Mesh t0 in Figure 4.
  This combines t1 and t2 in such a way that the alignment is localized in the upper-right and lower-left blocks of the rectangular domain. In the upper-left and lower-right blocks, the misalignment is the same as in Mesh t2.

5. Numerical Experiments and Discussions

As our first case, the contours of T are plotted in Figure 5 to demonstrate the numerical representation of the transition layer with regard to the grid resolution and the order of finite elements. κ_ξ is fixed at 10^3 and t_1 mesh is used. A lower conduction number is chosen here so that the plot contrast is clearer for a better view. Another reason is that when the anisotropy is relatively low, the transition layer is not sensitive to the type of meshes. We will discuss more about this later.

Note that there are 7 contour lines drawn in each sub-plot. Counting from color green to red, they are $T = 0.125, T = 0.25, T = 0.50, T = 0.625, T = 0.75$, and $T = 0.875$ contour lines, respectively. The 1st row corresponds to the linear elements with increasing grid resolution. As the grid gets refined, the layer is narrowed, but not significant. A dramatic improvement is found at the 2nd row where the second order elements are applied. At this row, one can see that the layer is much thinner. The 3rd row is obtained by the third order elements. Clearly the layer is narrowed down to another level. From this figure we can conclude that the proper resolution of the transition layer depends on the higher order elements other than on the grid refining.

The transition layer is introduced by the perpendicular conduction κ_η. It's width is denoted by wd. The numerical computation of this layer at high anisotropy can be difficult in the case when the computational grid is not

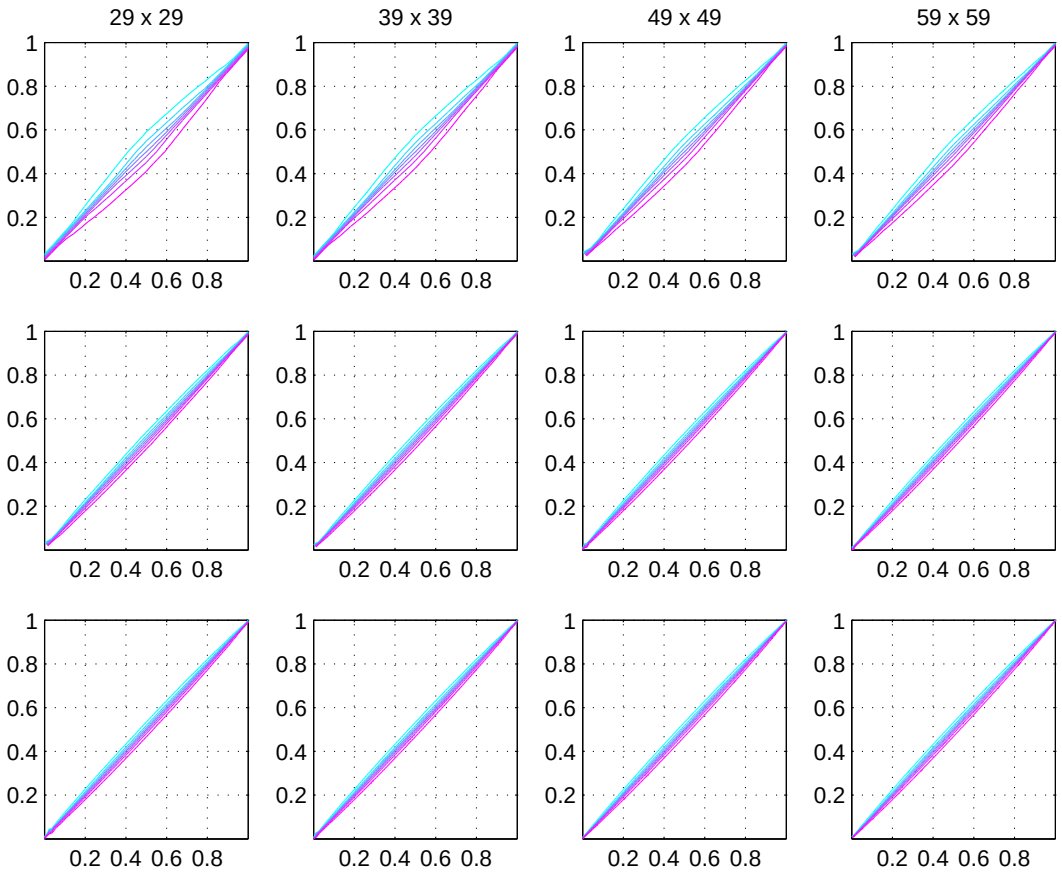

Fig. 5.

aligned with the strong transport direction, κ_ξ.

wd is plotted against the increasing anisotropy in Figure 6 for all the 3 types of meshes. The κ_ξ has the values $10^1, 10^2, 10^3, 10^4, 10^5, 10^6, 10^7, 10^8, 10^9$, while the grid resolution is fixed at 239×239. A large N_x and N_y is used here so that the solutions have surely converged with regarding to grid resolution. From the above conclusion, only the lump third order elements are applied this time. *Line RED* is for t_1 mesh; *Line GREEN* is for t_0 mesh; *Line YELLOW* is for t_2 mesh. The plot is divided into 2 parts due to the dramatic changes of the scale in wd. The first part is for $10^1 \leq \kappa_\xi \leq 10^5$. Its scale unit is $20\delta y$. The second part is for $10^5 \leq \kappa_\xi \leq 10^9$, and its scale is δy. Here $\delta y = 0.0014$. The area under each line represents the width calculated on each of the three types of meshes.

At small κ_ξ, $\leq 10^4$, the misalignment has a negligible effect. All three lines have the same bandwidth. When the anisotropy increases from $\sim 10^4$, the layer becomes thinner and the misalignment starts to affect this layer. At $\kappa_\xi \approx 10^4 - 10^5$, the effect is medium. wd keeps going down on t_1 mesh; while stays approximately at a level of $0.5\delta y$ on t_0 mesh, and $6\delta y$ on t_2 mesh. At large κ_ξ, $\geq 10^5$, the alignments become critical. The convergence of this layer

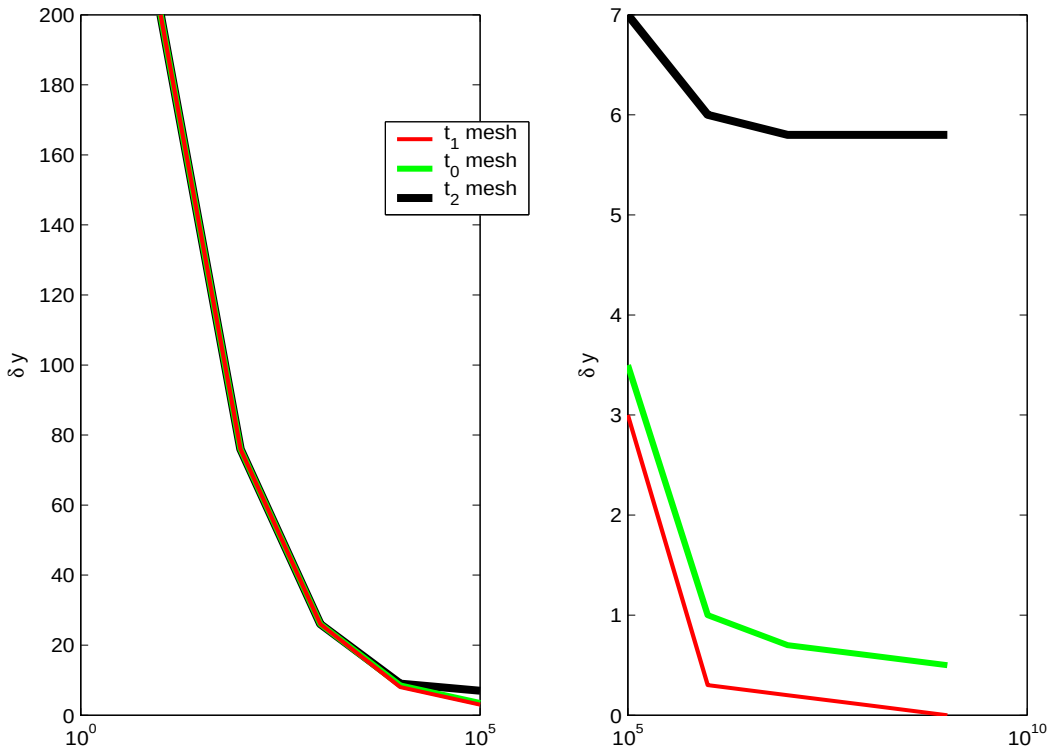

Fig. 6.

toward zero is only observed on t_1 mesh which has full alignments. On t_2 mesh with no alignments, wd stays as large as $5.8\delta y$. The width on t_0 mesh lies between t_1 and t_2. In all, wd on t_1 mesh drops correctly, while wd on the other 2 types of meshes failed to converge, particularly on t_2 mesh with no any alignments.

As our second case, the RMS of the error is plotted in Figure 7 against the grid resolution at $\kappa_{||} = 10^4$. t_0 mesh is used. Three lines are drawn to show how accurate the solution is calculated by linear (RED), lump 2nd order($GREEN$), lump 3rd order($YELLOW$) elements. Obviously the numerical solution is polluted by $\kappa_{||}$. It is verified again that the higher order elements are effective and necessary approaches in the existence of anisotropy.

In conclusion, the lump ho elements are proved to be effective approach to solve highly anisotropic transport problems with regard to timing and accuracy. Also in this study we found that grid alignment is essential to achieve better numerical accuracy even higher order method is used, and this is consistent with the conclusion made in [3].

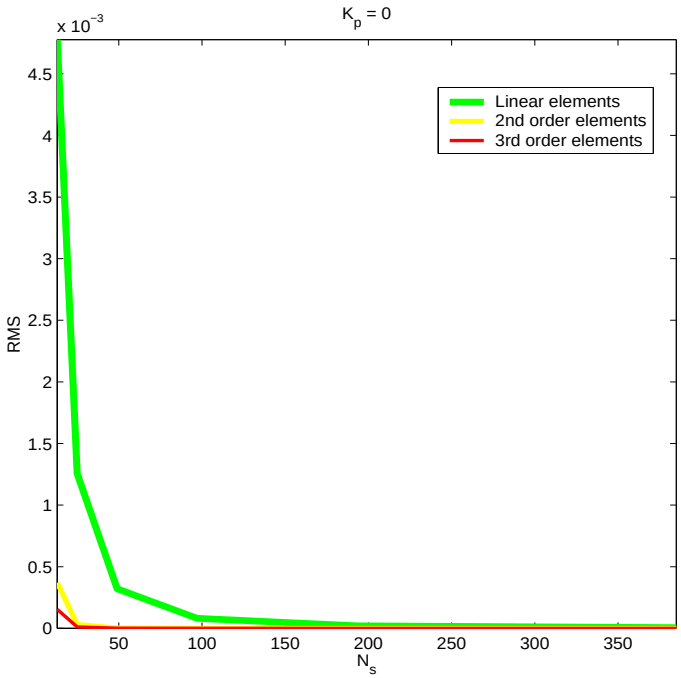

Fig. 7.

References

[1] W. Park et al, Nonlinear simulation studies of Tokamaks and STs, Nucl. Fusion **43**, 483 (2003).

[2] L. E. Sugiyama, W. Park, A Nonlinear two-fluid model for toroidal plasmas, Phys. Plasmas **7**, 11 (2000).

[3] M. V. Umansky, M. S. Day, and T. D. Rognlien, On Numerical Solution Of Strongly Anisotropic Diffusion Equation On Misaligned Grids, Numerical Heat Transfer: Part B: Fundamentals **47**, 6(2005).

[4] J. Chen, H. Strauss, S. Jardin, Solving Anisotropic Transport Equation on Misaligned Grids, LNCS **3516**, pp. 1076-1079, 2005.

[5] George Em Karniadakis and Spencer J. Sherwin, Spectral/hp Element Methods for CFD, Oxford University Press,2004.

[6] R. Vesey and D. Steiner, A Two-Dimensional Finite Element Model of the Edge Plasma, J. Comp. Phys. **116**, 300-313 (1994).

[7] R. Zanino, Advanced Finite Element Modeling of the Tokamak Plasmas Edge, J. Comp. Phys. **138**, 881-906 (1997).

[8] G. Cohen et al, Higher order triangular finite elements with mass lumping for the wave equation, Siam J. Numer. Anal. **38**, 2047-2078 (2001).

[9] J. Chen et al., Symmetric Solution in M3D, Computer physics communication **164**, 468-471 (2003).

[10] S. C. Jardin, A triangular finite element with first-derivative continuity applied to fusion MHD applications, J. Comp. Phys. **200**, 133-152 (2004).